# A 3D ERT study of solute transport in a large experimental tank

L. Slater [a,*], A. Binley [b,1], R. Versteeg [c,2], G. Cassiani [b], R. Birken [d,3], S. Sandberg [e,4]

[a]*Department of Geosciences, University of Missouri—Kansas City, 5100 Rockhill Road, Kansas City, MO 64110, USA*
[b]*Department of Environmental Science, Institute of Environmental and Natural Sciences, Lancaster, LA1 4YQ, UK*
[c]*Lamont-Doherty Earth Observatory of Columbia University, 61 Route 9W, Palisades, NY 10964, USA*
[d]*Witten Technologies Inc., 295 Huntington Avenue 203, Boston, MA 02115, USA*
[e]*Department of Geosciences, University of Southern Maine, 37 College Avenue, Gorham, ME 04038, USA*

## Abstract

A high resolution, cross-borehole, 3D electrical resistivity tomography (ERT) study of solute transport was conducted in a large experimental tank. ERT voxels comprising the time sequence of electrical images were converted into a 3D array of ERT estimated fluid conductivity breakthrough curves and compared with direct measurements of fluid conductivity breakthrough made in wells. The 3D ERT images of solute transport behaviour were also compared with predictions based on a 3D finite-element, coupled flow and transport model, accounting for gravity induced flow caused by concentration differences. The tank (dimensions $185 \times 245 \times 186$ cm) was filled with medium sand, with a gravel channel and a fine sand layer installed. This heterogeneous system was designed to complicate solute transport behaviour relative to a homogeneous sand tank, and to thus provide a challenging but insightful analysis of the ability of 3D ERT to resolve transport phenomena. Four ERT arrays and 20 piezometers were installed during filling. A NaCl tracer (conductivity 1.34 S/m) was injected and intensively monitored with 3D ERT and direct sampling of fluid chemistry in piezometers. We converted the bulk conductivity estimate for 250 voxels in the ERT imaged volume into ERT estimated voxel fluid conductivity by assuming that matrix conduction in the tank is negligible. In general, the ERT voxel response is in reasonable agreement with the shape of fluid conductivity breakthrough observed in six wells in which direct measurements of fluid conductivity were made. However, discrepancies occur, particularly at early times, which we attribute to differences between the scale of the image voxels and the fluid conductivity measurement, measurement errors mapped into the electrical inversion and artificial image roughness resulting from the inversion. ERT images revealed the 3D tracer distribution at 15 times after tracer injection. The general pattern and timing of solute breakthrough observed with ERT agreed with that predicted from the flow/transport modelling. However, the ERT images indicate a vertical component of tracer transport and preferential flow paths in the medium sand. We attribute this to transient vertical gradients established during tracer injection, and heterogeneity caused by sorting of the sand resulting from the filling procedure. In this study, ERT provided a unique dataset of 250 voxel breakthrough curves in 1.04 m³. The use of 3D ERT to

---

\* Corresponding author. Fax: +1-816-235-5535.

*E-mail addresses:* SlaterL@umkc.edu (L. Slater), a.binley@lancaster.ac.uk (A. Binley), Versteeg@ldeo.columbia.edu (R. Versteeg), g.cassiani@lancaster.ac.uk (G. Cassiani), r.birken@wittentech.com (R. Birken), sandberg@usm.maine.edu (S. Sandberg).

[1] Fax: +44-1524-593985.
[2] Fax: +1-914-365-8150.
[3] Formerly at Lamont-Doherty Earth Observatory of Columbia University, 61 Route 9W, Palisades, NY 10964, USA.
[4] Fax: +1-207-780-4347.

generate an array of densely sampled estimated fluid conductivity breakthrough curves is a potentially powerful tool for quantifying solute transport processes. © 2002 Elsevier Science B.V. All rights reserved.

## 1. Introduction

Surface and cross-borehole electrical measurements have been used to infer solute transport mechanisms in a variety of heterogeneous environments (Daily et al., 1992; LaBrecque et al., 1996a). Electrical resistivity tomography (ERT) refers to the inversion of a large number of four electrode resistance measurements to obtain images of resistivity (or conductivity, the reciprocal) distribution (Daily and Owen, 1991). Bulk conductivity as measured using ERT is closely related to fluid conductivity. If other factors controlling bulk conductivity are static in time, a sequence of ERT images can provide qualitative (and possibly quantitative) information on active transport processes (Slater et al., 1997). There are several arguments in favour of using ERT imaging for the investigation of solute transport. First, ERT imaging allows non-invasive, semi-continuous access to information on the transport in a way which does not influence the transport itself. In contrast, invasive sampling of fluid conductivity can disrupt the natural flow regime at the measurement location. Second, the information is potentially of much higher resolution (and essentially in 3D) than information which can be derived from well measurements. Third, the electrode spacing can be adjusted to provide information on solute transport at varying scales greater than the point measurement scale. As this scale provides spatially continuous data, the probability of missing a preferential flow pathway, quite possible when depending on isolated point measurements of fluid conductivity, is minimised.

There are several examples of the successful use of ERT for imaging transport processes (see for example, Daily et al., 1992; Slater et al., 1997; 2000). Electrical data are typically presented as a sequence of ERT images from which transport processes are inferred from changes in conductivity. In a recent study, the concept of treating a sequence of 2D ERT images as a large number of pixel breakthrough curves for inferring solute transport characteristics was demonstrated (Slater et al., 2000). Binley et al. (1996) also demonstrated this concept on soil cores. The density of pixels is greater than the sampling density realistically achievable with direct (invasive) methods of fluid conductivity measurement. The support volume of ERT measurements is the size of the pixel, which is controlled by ERT array geometry and acquisition parameters. It is generally larger than the support volume of direct solute measurements, which is controlled by the size of the conductivity cell or the extraction volume. Although the ERT measurement is averaged over a larger support volume, these previous papers suggest that ERT may provide significant additional insight into complex transport processes.

The 2D ERT data acquisition and analysis applied in Slater et al. (2000) and Binley et al. (1996) limited the application of this concept, as 2D inversion cannot resolve 3D electrical structure. Instead, images of quasi-conductivity change, normalised to a 2D image plane, were calculated to provide a qualitative assessment of how solute transport behaviour might vary on a 2D plane. Furthermore, the relatively low ERT measurement frequency in the work of Slater et al. (2000) meant that the pixel breakthrough response was only coarsely resolved. Importantly, it was not possible to assess the integrity of the resolved pixel breakthrough curves, as no direct measurements of time varying fluid conductivity were made.

The experiment described in this paper was designed as a follow up to Slater et al. (2000). Our key objectives were: (1) to thoroughly investigate the potential for resolving voxel (i.e. 3D as cubes as opposed to 2D rectangles) breakthrough curves from a time sequence of ERT measurements, and (2) to compare and contrast 3D ERT images of solute transport with those predicted from 3D solute transport modelling based on the hydrogeological data. Most

importantly, we investigate whether the concept of defining voxel breakthrough curves (Binley et al., 1996; Slater et al., 2000) is achievable. We utilise an experimental tank facility, designed for combined 3D hydrogeological and geophysical measurements. Piezometers were installed for direct measurement of fluid conductivity at points on key ERT image planes. We apply fully 3D ERT data acquisition and inversion procedures, with a high temporal measurement frequency, to quantify voxel bulk conductivity values. Significant differences between the ERT images of solute transport and the tracer distribution predicted from the flow/transport modelling occur and are considered. Assuming a simple relationship between bulk and fluid conductivity, we convert ERT voxels to equivalent fluid conductivity for comparison with directly measured values in wells. We obtain a reasonable agreement between the voxel breakthrough response and directly measured values, although discrepancies occur, particularly at early times. Reasons for this disagreement, as well as recommendations for future application of 3D ERT in solute transport characterisation, are discussed.

## 2. Experimental tank facility

### 2.1. Tank construction

The experiment was performed in a large non-metallic tank [dimensions $1.85 \times 2.45 \times 1.86$ m] constructed in the basement of the Henry Krumb School of Mines at the downtown Manhattan campus of Columbia University (Versteeg and Birken, 2001a,b). This facility affords high-resolution geophysical imaging of subsurface processes in custom designed large-scale physical models. The tank is constructed from high strength fibreglass (Extren 500), fibre-bolts and other non-metallic components. The tank can hold about 9 m$^3$ of material (e.g. over 20 tons of sand), which is moved via a powerful sand vacuum and a 2-ton overhead crane. The vacuum, attached to a 55-gal drum, is used to move sand, water and wet sand within, and out of, the tank. A tilting drum holder is used to pour sand through a funnel system into the modelling tank at a controlled speed and volume. Further details of this physical modelling facility are described in Versteeg and Birken (2001a,b).

For the experiment described here, ERT arrays and observation wells were secured in place, and the tank then filled with sand. Twenty 2.54-cm-diameter observation wells, screened along the entire length, were installed at locations shown in Fig. 1 prior to filling the tank. These relatively large wells were used to allow access with conductivity probes, transducers and water level indicators available for this study. Four ERT arrays were installed at the locations shown in Fig. 1. The sand was then slowly poured through the funnel system into the tank using the tilting drum and crane device. In parallel, two 10-cm-wide gravel screens were installed at the in- and outflow sides (Fig. 1). These screens were divided from the sand using a fibreglass mesh. Complete filling of the tank took approximately 10 h.

The tank was primarily filled with medium-grain sand, although two channels were constructed to provide heterogeneity. This heterogeneous system was designed to complicate solute transport behaviour relative to a homogeneous sand tank, and to thus provide a challenging but insightful analysis of the ability of 3D ERT to resolve transport phenomena. In particular, we intended the gravel channel to act as a preferential flow pathway, which would result in a distinct breakthrough response identifiable in the fluid conductivity measurements made in wells and in ERT voxel behaviour. The fine sand layer was installed in the hope that it would retard any density-driven flow, again manifesting itself in the voxel breakthrough behaviour. Summary physical properties for the medium sand forming the bulk of the tank, as measured in the laboratory, are shown in Table 1. At 42 cm from the tank bottom, a fine-grain channel (see Table 1 for physical properties) was constructed extending the length of the tank, about 25 cm wide and 15 cm high. At 85 cm from the tank bottom, a gravel channel was created extending from the inflow side wall to the tank centre, about 12 cm wide and 8 cm thick. This channel was composed of gravel in the size range 0.5–1.0 cm. Although physical properties of this material were not obtained in the laboratory, the flow modelling (described later) predicted a hydraulic conductivity ($K$) of 260 m/day, which is consistent with Hazen-type estimates based on empirical correlation between effective grain size and $K$. At 93 cm from the tank bottom, a cylindrical chamber (length 50 cm) was installed to allow injection of a saline tracer
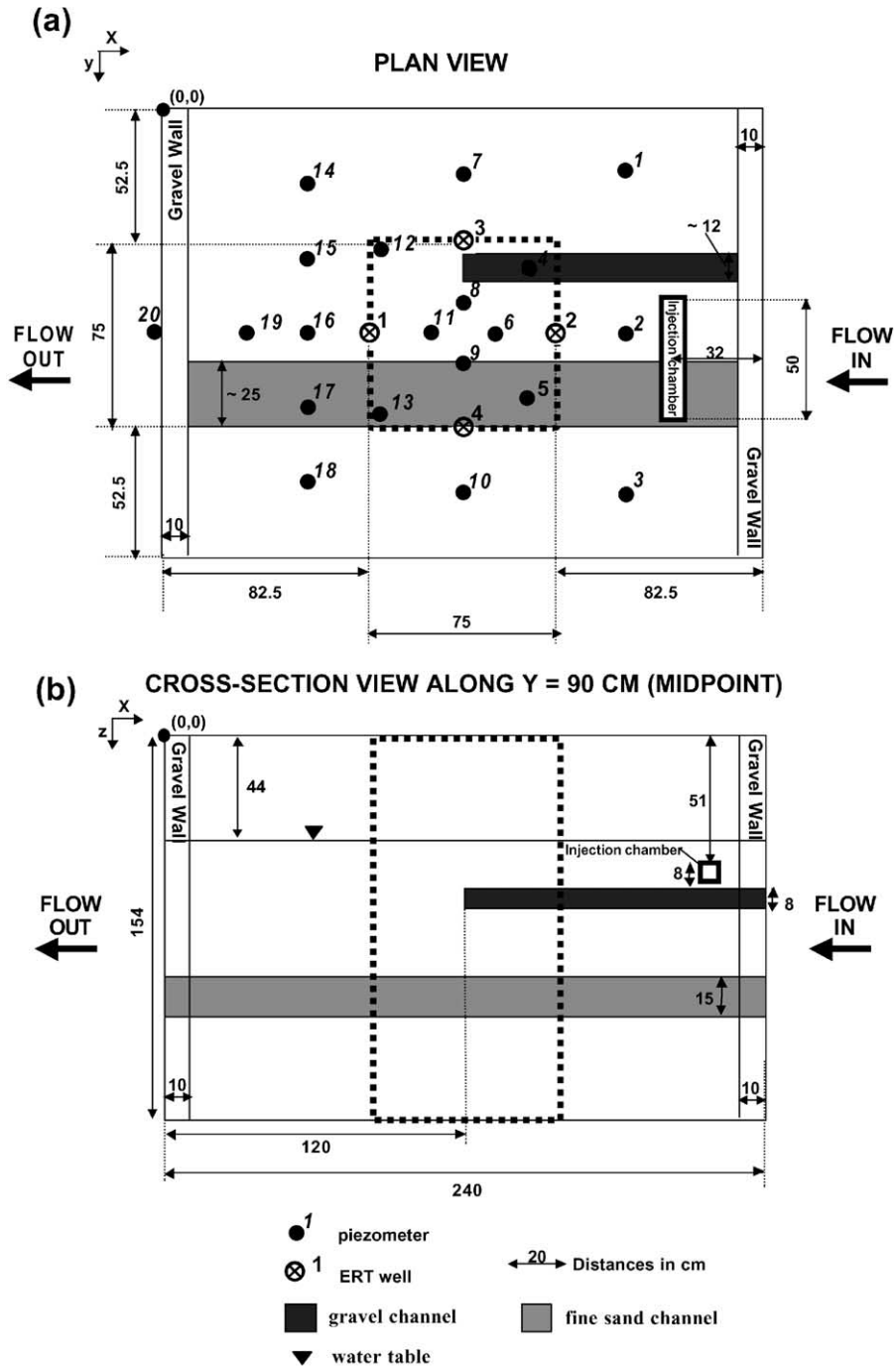
Fig. 1. Geometry of the experimental tank facility in (a) plan, and (b) cross-section, showing tank structure, ERT arrays, well installations, flow direction and location of tracer injection chamber. Tank is filled with medium grain sand, except for the gravel and fine sand channels shown. Note that the horizontal gravel and fine sand channels are not continuous in the $y$ and $z$ directions. The water level shown is that prior to the establishment of the hydraulic gradient used to generate the flow field, which involved lowering the water level at the outflow side by 3 cm.

Table 1
Laboratory measured physical properties of the medium sand used to fill the experimental tank and the fine sand layer installed

| Summary grain size | % finer than | |
| --- | --- | --- |
| Diameter (mm) | Medium sand | Fine sand |
| 0.02 | 0 | 8 |
| 0.06 | 0 | 15 |
| 0.2 | 4 | 56 |
| 0.6 | 65 | 82 |
| 2.0 | 96 | 100 |
| Other properties | | |
| Porosity | 0.38 | 0.31 |
| Formation factor | 4.3 | 6.0 |
| Hydraulic conductivity (m/day) | 15 | 1 |

The properties of the gravel channel, composed of gravel in the range 0.5–1.0 cm, were not measured. However, the flow modelling performed on the tank predicted a hydraulic conductivity of 260 m/day for the gravel channel.

beneath the water table (Fig. 1). This 8-cm-diameter PVC pipe was perforated with drill holes and covered with a fine mesh to prevent sand entering the chamber.

In addition to this primary heterogeneity, secondary heterogeneity undoubtedly occurred within the medium sand. We suspect that the simple method used to fill the tank, based on pouring dry medium sand from a tilted drum through a funnel and into the top of the tank, resulted in layers with significant fining upward sequences. An experiment conducted in a $50 \times 50 \times 75$-cm glass test tank supports this premise. This test tank was filled using the same method and with the medium sand used in the study described here. Sorting of the sand and formation of macrostructure, primarily layers of relatively coarse or fine sand, was unavoidable using this method of sand emplacement. As a result of this, the porosity of the medium sand undoubtedly varies around the laboratory-measured value (Table 1). As, in clay-free systems, porosity exerts a primary control on $K$, we expect that variability in $K$ also exists within the medium sand. It was not possible to assess this in situ spatial variability in porosity or $K$ in the medium sand. A simple calculation, obtained knowing the total tank volume and the volume of water added to insure saturation, yielded a bulk porosity of the tank of 42%. This high value, relative to that obtained in the laboratory, may reflect the loose packing of the sand in the tank, relative to that in the laboratory. In fact,

the overall thickness of the tank material (prior to addition of water) was observed to reduce from 150 cm immediately after filling to 147 cm after 3 days, due to natural settling and compression of the loosely packed dry sand.

## 2.2. Hydrogeology and tracer sampling

Standard 2.54-cm PVC pipes were installed close to the tank bottom at the inflow and outflow sides of the tank. The tank was slowly saturated by supplying water (conductivity 0.008 S/m) at the inflow pipe via a constant head reservoir, whilst keeping the outflow pipe closed. Rather than supply direct from a tap, all input water was first stored in a storage container with large surface area, to minimise trapped air bubbles from being introduced into the tank. Saturation was achieved incrementally, through successive additions of approximately 250 l of water. After each incremental addition, the water levels in observation wells were monitored until a flat potentiometric surface was achieved, i.e. water levels in observation wells equilibrated with the level of the constant head reservoir. At this point, the constant head reservoir was raised to add the next 250-l increment of water and the monitoring repeated. This process was continued over a period of 26 h, until the water level reached $z = 110$ cm (Fig. 1). This procedure was expected to provide a close approximation to saturation for the sand and gravel environment used in this experiment, and to minimise variability in saturation across the tank caused, for example, by trapped air pockets. In order to accommodate operator access to the tank, the uppermost 44 cm of the tank was left unsaturated.

A steady-state flow field was established in the tank prior to tracer injection. The constant head reservoir used to fill the tank at the inflow side was maintained at $110 \pm 0.5$ cm above tank bottom. This reservoir was supplied with tap water of conductivity 0.008 S/m. The outflow pipe was opened, and a valve was used to maintain a constant head on the outflow at $107 \pm 0.5$ cm. The flow rates on the inflow and outflow pipes were monitored until they were approximately equal ($\pm 0.5$ l/h), at which point a steady-state flow field was assumed. This flow field was then maintained for an additional 8 h prior to tracer injection, and for the remainder of the experiment. The head drop of 3 cm across the tank resulted in a

flow rate of about 18 l/h during the tracer experiment. Applying Darcy's Law, we calculate a bulk hydraulic conductivity for the tank material of 16 m/day, which is surprisingly close to the laboratory measured value for the medium sand. Of course, this calculation does not consider the effect of the gravel channel, fine sand layer or the heterogeneity introduced by the tank filling procedure. For a head drop of 3 cm and a bulk porosity of 42%, the bulk seepage velocity estimate is 52 cm/day.

Following the collection of background ERT and fluid conductivity data, 6 l of NaCl tracer with a concentration of 6.4 g/l (relative density of 1.0064) and conductivity of 1.34 S/m was added to the injection chamber 15 cm below the water surface (Fig. 1) over a 3-min period. The tracer best approximates an instantaneous slug injection, although elevated water levels in two riser pipes extending from the injection chamber to the surface were observed during injection and probably induced some downward tracer transport in the initial stages following tracer input.

ERT, fluid conductivity and water level measurements were made as frequently as practically possible over a 224-h experimental period following tracer injection. We obtained a total of 25 frames of ERT data and 20 frames of fluid conductivity sampled in wells. Fluid conductivity in wells was measured at multiple levels in each well during the early hours of the experiment. Early results from the ERT measurements (processed during the experiment) and the fluid conductivity measurements were then used to estimate good locations (in the vertical) in wells for the comparison between ERT voxel breakthrough behaviour and breakthrough determined from direct measurements. At this point, the conductivity probes were kept in place, in order to minimise mixing of the fluid in the wells. However, we expect that, due to the screening of the wells over the entire length, some mixing within the wells occurred. Consequently, the fluid conductivity measurements in the wells cannot strictly be considered a representative point value. As the ERT voxels are also an integrated response over a significant volume, it is still appropriate to compare the two breakthrough curves, recognising that differences in the scale of the measurements will affect the interpretation. As no vertical hydraulic gradients were established in the tank (other than for a short time

period at the injection chamber during tracer injection), it is unlikely that the screened wells acted as preferential flow paths. Our ERT images, and measurements of fluid conductivity in wells after the experiment, support this statement.

## 3. Electrical resistivity tomography

The concepts of the ERT method are well described in the geophysical literature (see for example, LaBrecque et al., 1996b). Resistance measurements (the ratio of the voltage between an electrode pair to the current injected between another electrode pair) are made for a large number of sets of four electrodes placed in boreholes or at the surface. Given these measurements, it is possible to solve numerically for a conductivity distribution that results in a set of calculated resistance measurements which best fits with the measured response. The numerical solution applied for the ERT inversion incorporates 3D finite element (FE) forward modelling and minimisation of a weighted, regularised objective function. This modelling takes into account the impermeable boundary conditions at the walls and base of the experimental tank.

Cross-borehole electrical measurements were made using stainless steel electrodes placed on four ERT arrays (ERT 1–4 on Fig. 1). Electrodes were spaced at a 15-cm interval on each array. The lowermost electrode on each array was 4.5 cm above the tank bottom. Cross-sections along $y = 90$ cm (Fig. 2a) and $x = 120$ cm (Fig. 2b) illustrate the location of electrodes in relation to tank structure and show the geometry of the FE mesh used in the 3D ERT modelling. Measurements were made using a programmable multi-electrode system (a 32-channel multi-electrode, single channel Iris Syscal R1+). The high contact resistance with the dry sand prevented the use of the uppermost two electrodes on each array.

It is necessary in ERT experiments to consider the optimum set of four electrode measurements. Given 32 electrodes, a total of 464 independent measurements exist when using a circulating dipole (nearest neighbour) measurement scheme (Xu and Noel, 1993). With this configuration, adjacent electrodes are used as voltage pairs and current injection pairs. In theory, these measurements will contain all the
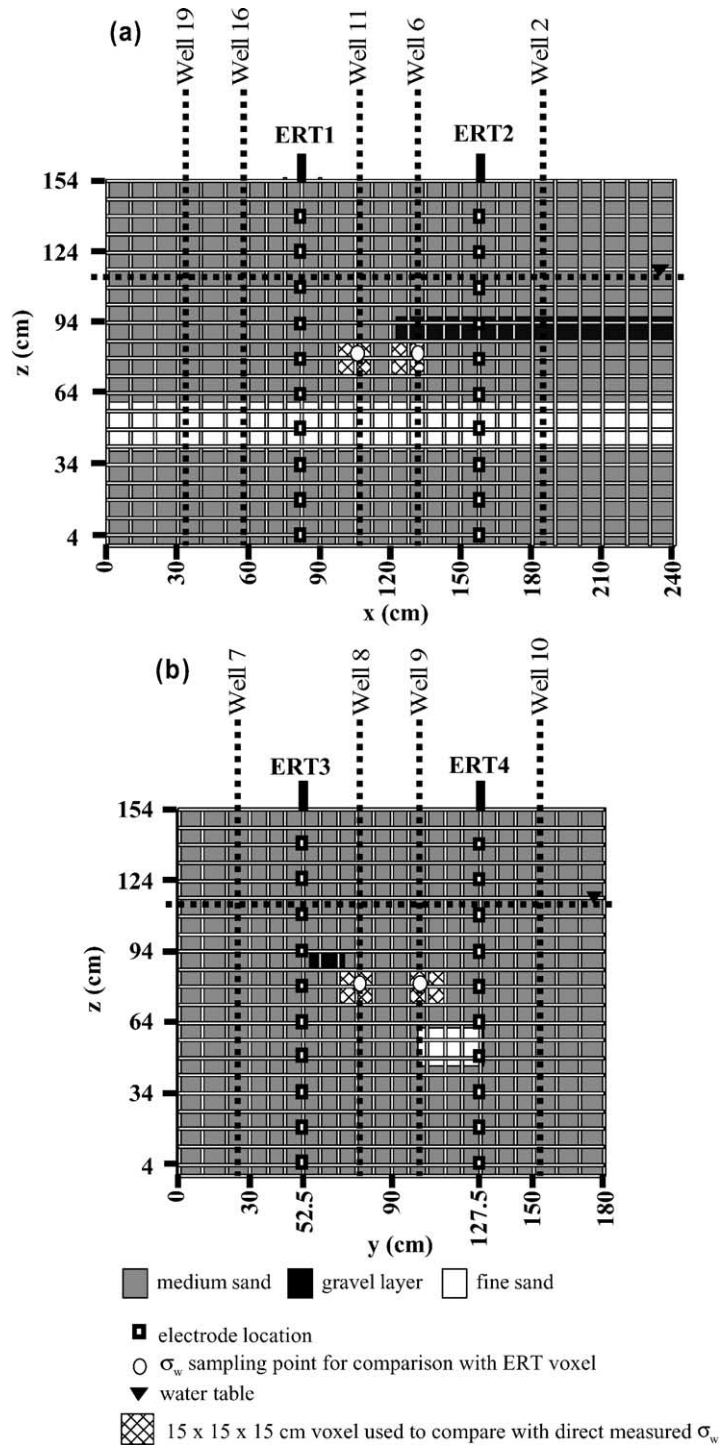
Fig. 2. Location of electrodes and geometry of ERT finite element mesh along (a) $y = 90$ cm and (b) $x = 120$ cm. Tank structure is shown.

information on the resistivity structure obtainable from 32 electrodes. In practice, this schedule is ineffective, as small voltages obtained between closely spaced potential electrodes result in low signal-to-noise ratio. To overcome this, a circulating schedule, in which one or more electrodes are skipped, was utilised here. On each image panel, a 'skip 1 electrode' and a 'skip 2 electrode' circulating schedule was applied (Fig. 3). A single 3D ERT dataset was created from four electrode measurements that utilised electrodes in all four boreholes. Cross-borehole measurements were made using six panels. The panels are defined in terms of the ERT boreholes and are 1–2, 3–4, 1–3, 2–3, 1–4 and 2–4, where, for example, panel 1–2 defines a set of meas-

urements that utilised electrodes in boreholes 1 and 2. A single 3D dataset consisted of a total of 960 measurements. As the number of conductivity parameters to be resolved is slightly greater than the number of measurements (1392), this is a slightly underdetermined problem, suitable to the ERT inversion method applied here.

Data acquisition time is a crucial factor in ERT imaging. Ideally, the ERT image will represent a snapshot image of tracer distribution at a point in time. One of the main points which is unclear in time lapse geophysics is both the effect of temporal aliasing and the effect of distributing our measurements over a long period of time compared to the processes. Con-
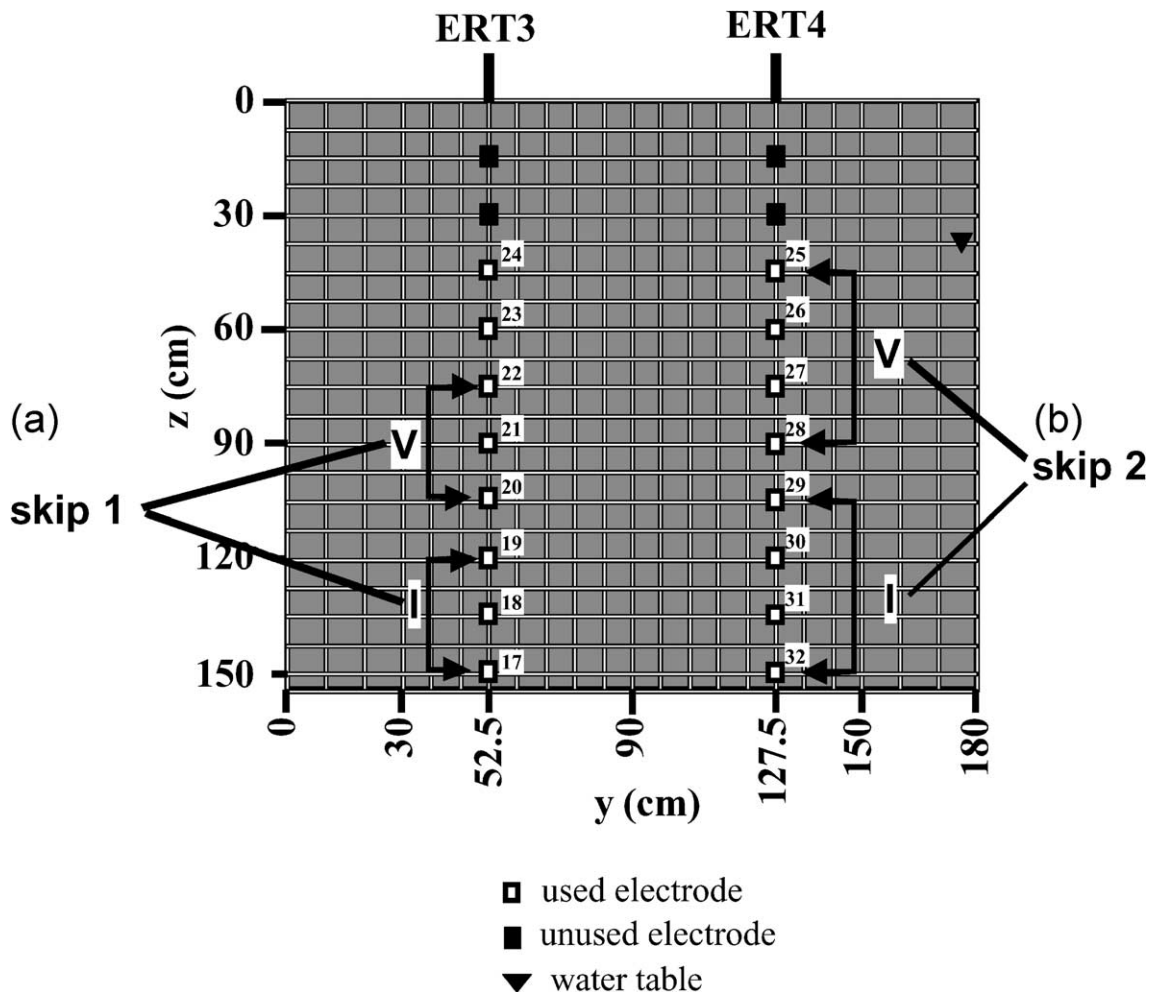


Fig. 3. ERT measurement schedules used in 3D data collection (a) 'skip one', (b) 'skip two' circulating dipoles.

ceptually, we expect excessively slow data collection rates, relative to the speed of solute movement, to result in a blurred representation of solute distribution.

Using the estimated bulk tank seepage velocity of 52 cm/day, the tracer was estimated to move 3 cm during data acquisition (90-min interval), equivalent to half a voxel in the ERT FE mesh (a distance below the resolution of this method). Greater movement between images was anticipated for tracer transported in the gravel layer and any vertical transport due to density effects or transient gradients established during tracer injection.

Quantification of data noise is an important factor in ERT. LaBrecque et al. (1996b) show that over-estimation of data noise results in excessively smooth resistivity structure. In contrast, underestimation of data noise results in artificial image structure unrelated to the resistivity distribution. Noise estimation can be performed based on repeatability or reciprocity checks (Binley et al., 1995). Reciprocity is a better measure but is time intensive as the entire set of measurements must be repeated with the current and potential electrode pairs reversed. In this study, a combination of repeatability and limited reciprocity tests was performed to characterise data noise. A Gaussian noise distribution with a maximum relative error of 3% fitted the data and resulted in satisfactory inversion performance.

The spatial resolution of electrical imaging is not defined analytically as it is an unknown function of many factors including measurement error, electrode geometry, measurement schedule (number of independent measurements) and the resistivity distribution (Daily and Ramirez, 1995). The spacing between electrodes and distance from current sources exert a fundamental control on resolution. A useful numerical computation is the "resolution matrix" (Slater et al., 2000), which quantifies the relative resolution in any image plane. The resolution matrix can detect bias in image resolution caused by the selected sequence of ERT measurements. In this study, resolution above 110 cm (the unsaturated part of the tank) is poor, due to the distance from active electrodes. Between 0 and 110 cm (the saturated part of the tank), the resolution uniformly decreases away from the arrays, such that resolution is poorest at the centre of the images. Further discussion of ERT resolution is given in LaBrecque et al. (1996b) and Daily and Ramirez (1995).

The FE mesh we used to forward model the electrical response contains 2000 voxels of dimensions $7.5 \times 7.5 \times 7.5$ cm within the imaged area (see outlined box in Fig. 1). The inversion dictates that the best possible image resolution is the size of one inverted voxel. In order to simplify and accelerate the ERT inversion, integrated voxels (dimensions $15 \times 15 \times 15$ cm) were formed by averaging eight adjacent elements of the finite element mesh i.e. one integrated voxel contains $2 \times 2 \times 2$ finite elements (Fig. 2). This gives 250 integrated ERT voxels within the central portion of the tank, as defined by the dashed box in Fig. 1. The ERT support volume is considerably larger than that for the direct measurement of fluid conductivity in the wells. However, the ERT voxels are a spatially extensive and continuous set of sensors of changes in fluid conductivity.

## 4. Solute transport modelling

FEMWATER (Lin et al., 1997), a variably saturated flow and transport FE model, was used to model solute transport in this tank. The simulation was carried out for coupled flow and transport, i.e. including the gravity effect of NaCl concentration on the flow field. For simplicity, the upper unsaturated 35 cm of the tank was not included in the modelling. The primary tank lithology shown in Fig. 1 was simulated in the modelling. Saturation was assumed below the water table. The water levels in the piezometers before injection were sufficiently close to those expected in a homogeneous tank, not to warrant the need for a calibration of the model against the initial, steady-state flow conditions. This is hardly surprising, since head values are notoriously insensitive to heterogeneities in the subsurface, and in fact the inverse problem of retrieving the $K$ field from the head values is severely ill-posed.

It was necessary to assign the hydraulic conductivity of the sand as 29 m/day (compared to 15 m/day measured for a repacked sand sample and 16 m/day bulk estimate for the tank) to reproduce the breakthrough response observed in piezometers (Fig. 1). It is impossible to exactly replicate the filling procedure used in the tank, the compaction observed after filling and the variation in $K$ that probably occurred within the medium sand due to the macrostructure resulting from the filling process. This reflects the complexity of

extrapolating lab measurements to field measurements, even in a very well-controlled situation such as this. The hydraulic conductivity of the gravel layer and fine sand layer was modeled as 256 and 1 m/day, respectively. The longitudinal and transverse dispersivity were chosen to represent the low end of the range of possible values, being 2 and 0.5 cm, respectively.

The head difference established prior to tracer injection was the forcing boundary condition for flow. Tracer injection was simulated by setting the initial NaCl concentration equal to the injected solution concentration (6.4 g/l) in the model region including and immediately surrounding the injection chamber (Fig. 1). The volume of porous medium flooded by the injection solution was calculated from the porosity estimates. The simulation time zero corresponds to the end of the injection. This procedure neglects the possible transient gradients induced by the height of the tracer in vertical pipes that extend from the tank surface to the injection chamber. The total simulation time was 48 h. The model consisted of 10,000 nodes and 17,000 elements, resulting in 20,000 unknowns (pressure and concentration at each node) which were solved for in an iterative manner using the 3D flow and transport equation.

## 5. Results

### 5.1. Voxel response

In the absence of significant matrix conduction and assuming total saturation, the ERT voxel bulk conductivity $\sigma_b$ is directly related to voxel fluid conductivity $\sigma_w$ through Archie's Law (1942),

$$\sigma_w = F\sigma_b, \tag{1}$$

where $F$ is the formation factor, a function of effective porosity and other physical properties related to the packing. Matrix conduction is typically significant when clay minerals are present or when $\sigma_w$ is very low. Eq. (1) is considered to apply in this experiment, as a measurable clay/silt fraction is absent (Table 1). The apparent formation factor of each image voxel was estimated from Eq. (1) using the inverted voxel $\sigma_b$ obtained for the pre-injection ERT dataset. Fluid conductivity measurements made in all 20 wells (Fig.

1) prior to tracer injection showed a uniform increase from about 0.014 S/m at the inflow side of the tank to about 0.02 S/m at the outflow side. We assume that this resulted from the progressive washing off of salts from the sand and gravel, as water was transported through the tank under the established flow field. In the central portion of the tank imaged with ERT, $\sigma_w$ ranged from 0.0164 to 0.0175 S/m, as measured at wells 5–6, 8–9, 11 and 13 (Fig. 1). A $\sigma_w$ estimate was obtained for each voxel and applied in Eq. (1).

Fig. 4 shows the voxel estimated $F$ for image plane 3–4, with $F$ ranging from 2.8–5.0. A similar range was observed for image plane 1–2. The formation factor of the medium sand was measured in the laboratory as 4.3. How well Fig. 4 reflects variability in the packing of the material is questionable. This small range of $F$ may not be significant given the image uncertainty due to measurement errors, nonuniqueness in the inversion and unpredictable changes in fluid conductivity. However, some of the variability observed in Fig. 4 is consistent with that expected from the tank construction. Higher formation factors are generally observed at depth, which may relate to generally greater packing due to the weight of overlying sand. Furthermore, the fine sand layer is imaged as a region of relatively high $F$, whereas the gravel channel is a zone of low $F$.

We used the voxel estimates of apparent $F$ to convert the time sequence of ERT image voxels to equivalent fluid conductivity, enabling comparison between voxel response and directly measured $\sigma_w$ during solute breakthrough. Fig. 5 shows ERT-estimated voxel $\sigma_w$ behaviour during the experiment compared with $\sigma_w$ behaviour obtained from direct measurements at $z = 79$ cm in six wells (5–6, 8–9, 11 and 13) installed within the imaged volume. Again, it is important to appreciate the different support volumes of the two measurements. Whereas the direct measurements of $\sigma_w$ are quasi point measurements (as we measure in the well we expect some mixing), the voxel values represent the volume-averaged conductivity for 3375 cm$^3$ of material centred on the $\sigma_w$ measurement (Fig. 2). As previously discussed, this scale difference results from the limitations imposed on ERT resolution by the speed of data acquisition hardware relative to sampling frequency, and practical limitations on computational demands for the inversion.
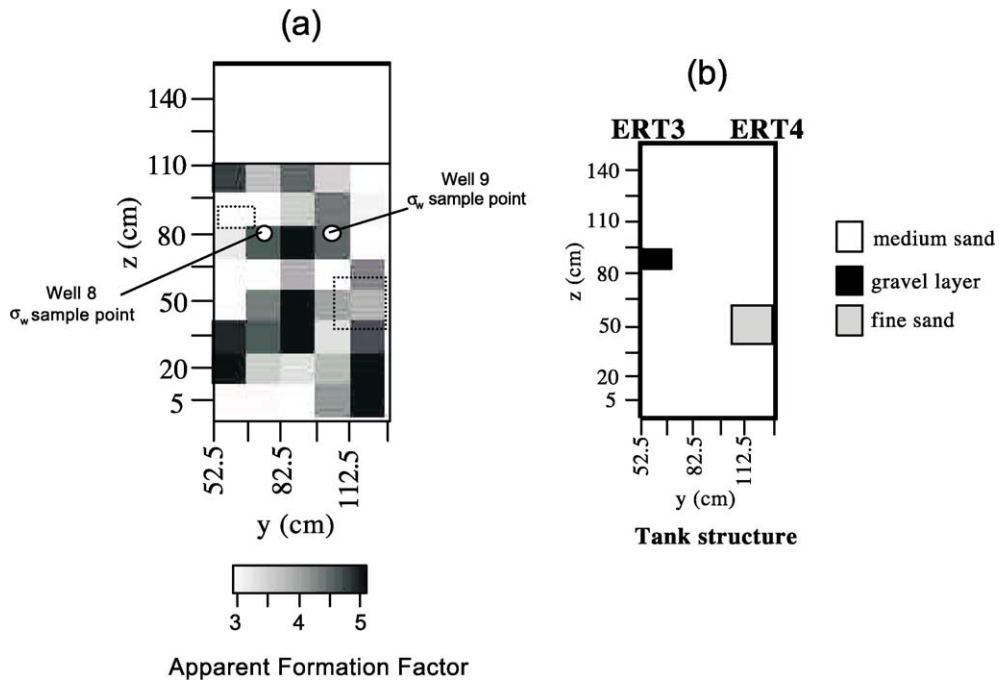
Fig. 4. (a) Apparent formation factor calculated for image plane $x = 120$ cm, excluding the region above the water table (110 cm). (b) Basic known tank structure for comparison. Apparent formation factors were calculated using the pre-injection 3D ERT inversion and $\sigma_w$ estimates for each voxel obtained from pre-injection sampling at wells. The location of $\sigma_w$ sampling points during tracer monitoring in this image plane is also shown.

Given this scale difference, the correlation between ERT and directly measured $\sigma_w$ is in general good. Direct $\sigma_w$ measurements were not made during the first 20 h of monitoring (we chose to concentrate on continual ERT monitoring to catch early breakthrough caused by the gravel layer), thus preventing accurate comparison of breakthrough behaviour between these times. ERT voxel response at wells 11, 6 and 13 closely follows directly measured $\sigma_w$. At Well 8, the correlation is good, except between $t = 20$ and 30 h. At Well 5, the first breakthrough time occurs at about $t = 25$ h for both ERT voxels and directly measured $\sigma_w$, although the amplitudes of the two curves are inconsistent between $t = 40$ and 80 h. At Well 9, the voxel response is more complicated than the direct measurement. These discrepancies may reflect the difference in support volume between the two measurements, secondary effects caused by minor temperature variations or measurement noise mapped into the ERT inversion. The rough ERT response at certain

voxels may also result from the nature of inversion routine applied here, which does not incorporate a smoothness-constraint on the time dimension. The implications of this are further considered in the discussion. However, the general agreement observed between ERT-estimated voxel $\sigma_w$ and directly measured $\sigma_w$ encourages our use of the 250 ERT voxels within the central portion of the tank for understanding solute transport in this tank.

### 5.2. ERT images of tracer transport compared with hydrological modelling

The results presented here are confined to the centre portion of the tank defined by the dashed box in Fig. 1 as the ERT inversion is insensitive to the conductivity distribution outside of this volume. The coupled flow and transport simulation results are presented for panel $x = 1.2$ m in Fig. 6. To simplify the comparison between datasets, the nodal values have been up-scaled (by
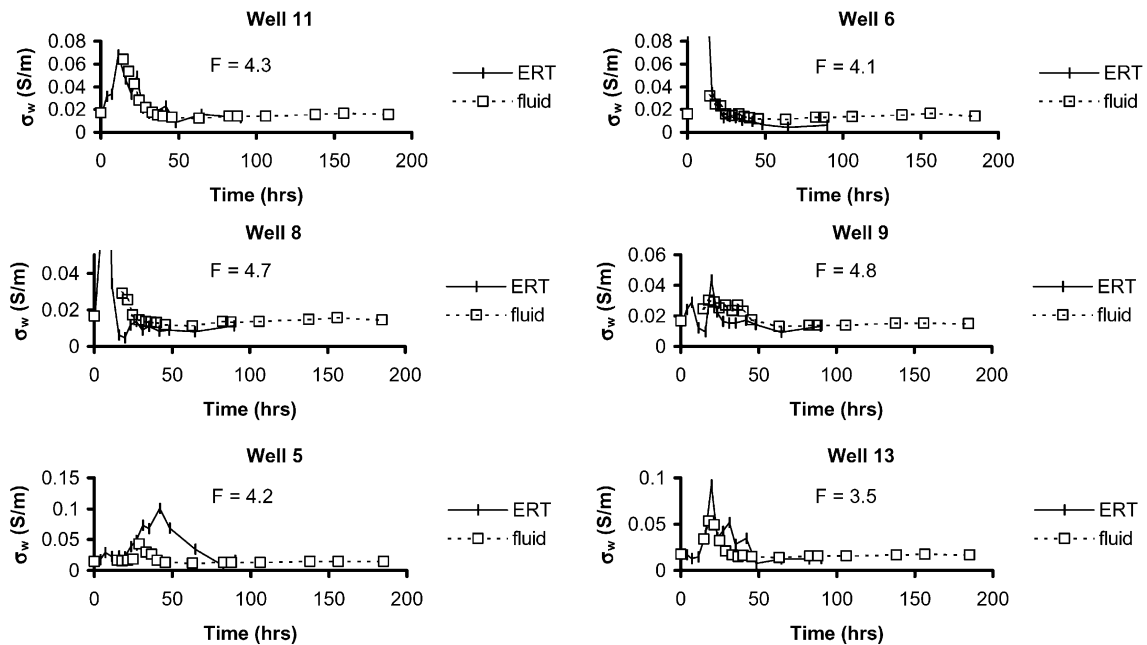
Fig. 5. ERT-derived voxel breakthrough curves compared with $\sigma_w$ curves obtained from direct measurements in six wells installed within the imaged volume. Formation factor ($F$) used in conversion from bulk to fluid conductivity (determined from background images) is shown. The conductivity probe was at $z = 79$ cm in all wells. Refer to (Figs. 1, 2 and 4) for sampling locations relative to the ERT mesh.

averaging nodal values) to the equivalent scale of the inverted ERT voxels ($15 \times 15 \times 15$ cm). Note that the hydrological simulation applies only to the saturated part of the tank. The result shows several important features. Firstly, early breakthrough is clearly seen at 7.1 h after injection and corresponds with the location of the permeable gravel channel location. This breakthrough is first observed at $t = 3.7$ h but is not resolvable on the scale of this image. Secondly, delayed breakthrough within the medium sand occurs after 11.2 h with a peak solute concentration at 19.7 h. This delayed plume is dispersed over a $60 \times 60$-cm area in this image plane, but skewed away from ERT 3. Thirdly, only minimal vertical transport, induced by the density contrast between tracer and tank fluid at early time, is evident at the centre of the section, where the plume shows a slight downward wedge. Dilution of the tracer rapidly eliminates the density-driven flow.

Electrical images of ERT-estimated $\sigma_w$ are shown for plane $x = 120$ cm in Fig. 7a. The image response is consistent with the modelling in a number of aspects. Firstly, voxel response in the vicinity of the gravel channel is observed at only 3.7 h and is strongest after

7.1 h. However, the magnitude of ERT-estimated $\sigma_w$ is greater than the magnitude predicted from the hydrological modelling. This is expected, as $F$ assigned to the tank (based on the medium sand filling the majority of the tank) is greater than the unknown $F$ of the gravel, leading to an overestimate of $\sigma_w$ from Eq. (1). A second consistency between ERT observations and hydrological model results is the timing of breakthrough within the sand. By 11.2 h, delayed breakthrough is detected at voxels towards the tank centre, peaking at 19.7 h. The magnitude of the voxel response (where tracer is detected) is broadly comparable with that predicted from the transport modelling (in this case the formation factor used is appropriate). Although the dispersivity values assigned in the hydrological modelling represent the low end of the possible range of values, the ERT resolved tracer breakthrough in the sand appears more localised relative to the disperse plume predicted from the transport modelling.

Two important differences between the ERT images of solute breakthrough and the breakthrough predicted from the transport modelling exist. Firstly, a vertical component of flow is imaged with ERT (compare for
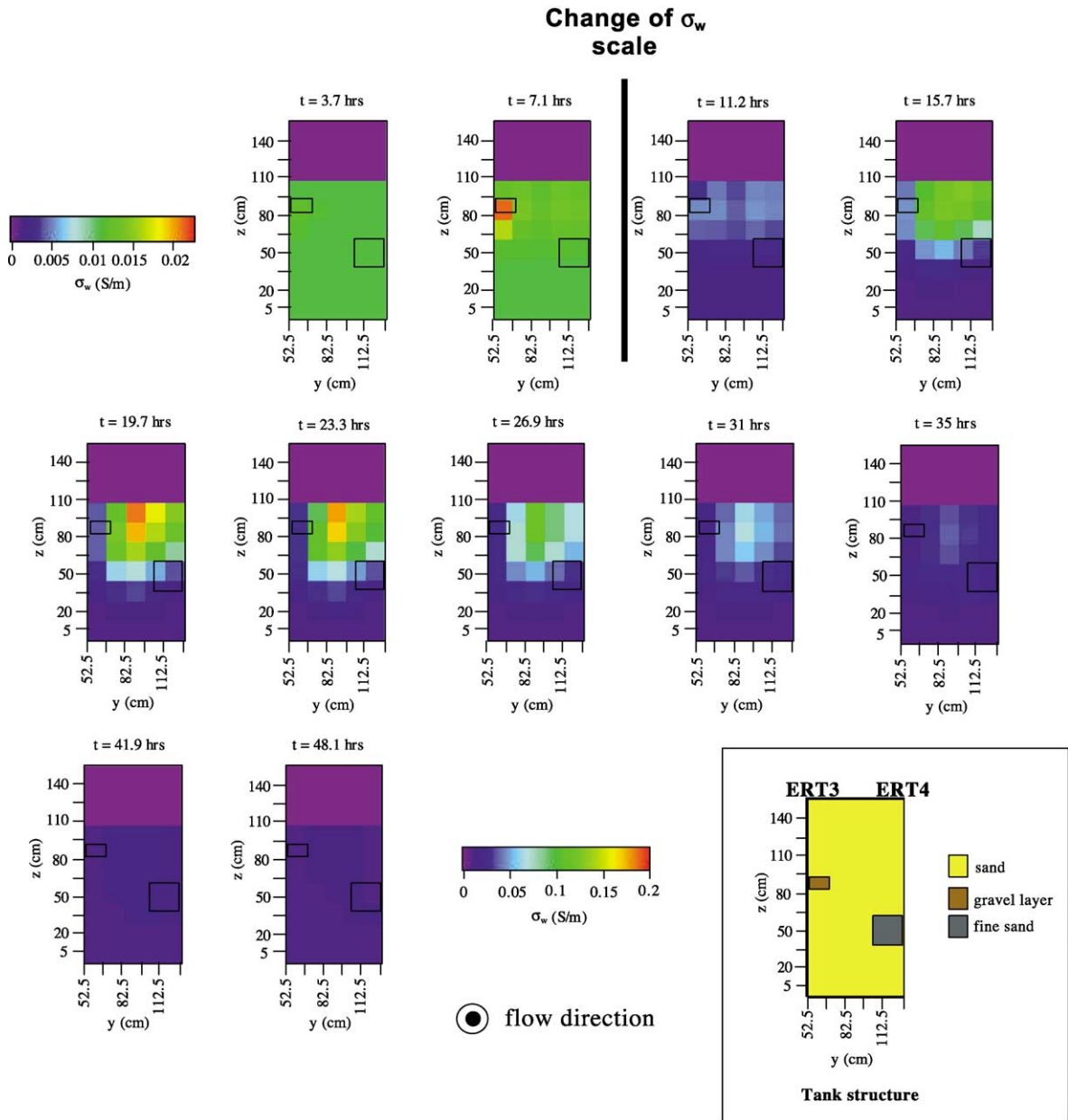
Fig. 6. 2D slices of $\sigma_w$ obtained from the coupled flow and transport modelling for image plane $x = 120$ cm. Note that the first two times are plotted using a narrow range of $\sigma_w$ in order to illustrate the predicted early breakthrough at the location of the gravel channel. As the unsaturated region (above 110 cm) is not included in the modelling, $\sigma_w$ above 110 cm is set to zero.

example the centre of tracer mass at $t = 26.9$ h in Figs. 6 and 7a). The transport modelling predicts that density effects can only explain ~ 5 cm of the ~ 30 cm of sinking suggested by the ERT images. The electrical

response along $y = 90$ cm (Fig. 7b) emphasises this apparent sinking. Here, early breakthrough associated with the gravel layer is obvious. Delayed breakthrough within the sand is apparent from $t = 11.2$ h with a
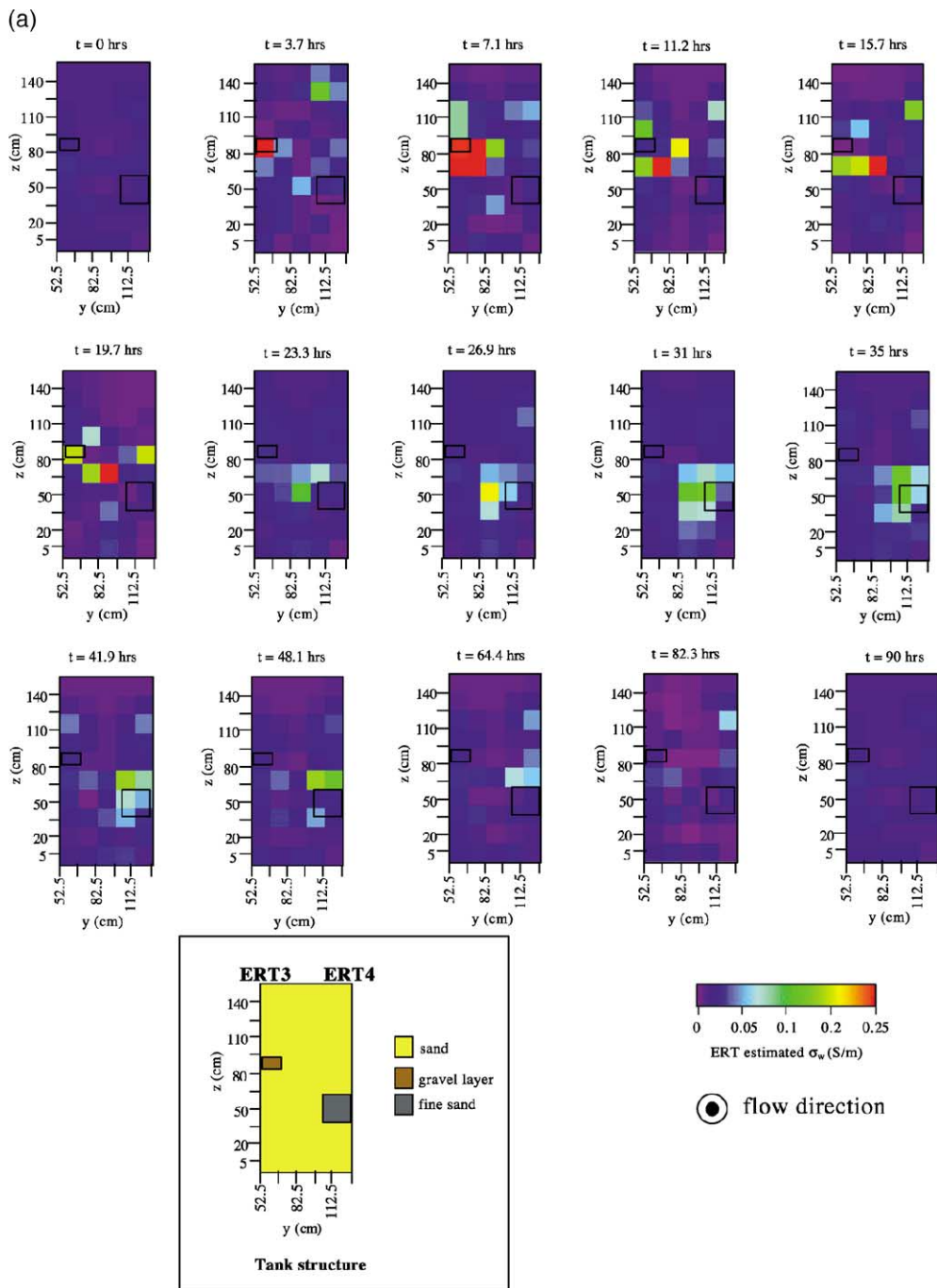
Fig. 7. (a) 2D slices of ERT-estimated $\sigma_w$ at $x = 120$ cm shown for 15 frames of the tracer experiment. Note that the gravel layer is not continuous in the $x$ direction (see Fig. 1). (b) ERT-estimated $\sigma_w$ at $y = 90$ cm shown for 15 frames of the tracer experiment. Note that the fine sand and gravel layers are offset from the image plane by approximately 20 cm and not continuous in the $y$ direction (see Fig. 1).
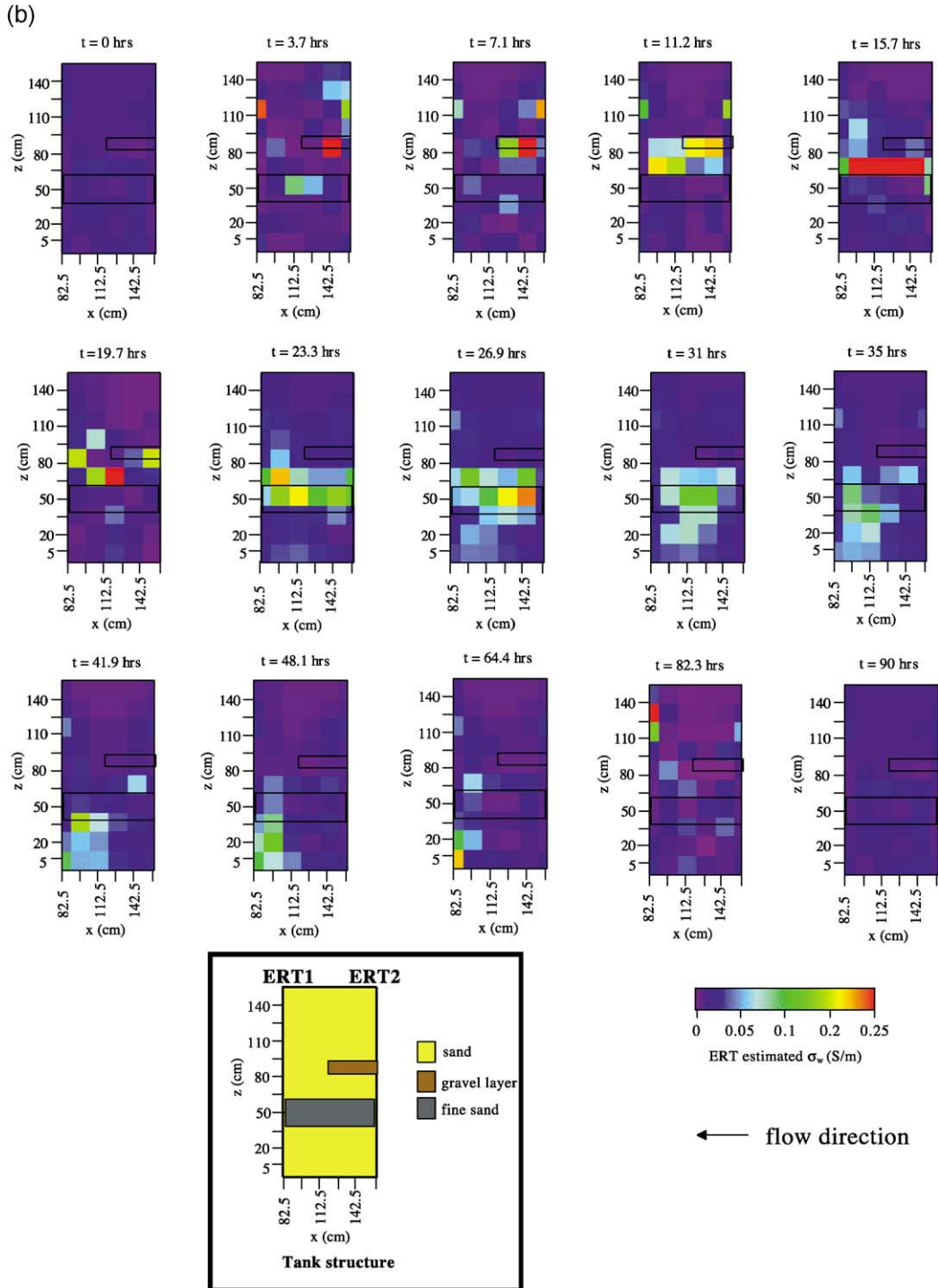
Fig. 7 (*continued*).

suggested vertical component of flow most apparent between $t = 19.7$ and 64.4 h. Note that the fine sand layer is not continuous in the $y$ direction and is offset by 20 cm from the tank centre (therefore, it is not a barrier to the sinking in this section). The second major difference between the ERT images and the solute modelling is the delayed breakthrough between $t = 35$ and 48.1 h observed above the fine sand channel in the ERT images.

## 6. Discussion

The generation of ERT voxel breakthrough curves is a potentially powerful approach to assist solute transport modelling. A densely sampled, spatially continuous mesh of breakthrough curves is not easily obtained using direct measurements of $\sigma_w$. This experiment investigated the utility of 3D ERT imaging to define a 3D mesh of voxel breakthrough curves by comparison with direct measures of $\sigma_w$ at wells within the ERT mesh. In general, we observe a good agreement between ERT voxel breakthrough curves and the direct observations made at wells. The correlation is by no means perfect: we attribute the differences to numerous factors, including (1) differences in the support volume of the two measurements, (2) inaccuracies in the estimation of the formation factor required to convert voxels from bulk conductivity to fluid conductivity, (3) measurement errors and their effect on ERT images, (4) non-uniqueness of the 3D inversion, and (5) limitations of the inversion routine as applied to temporal datasets. Despite these limitations, we feel that Fig. 5 illustrates the potential of the 3D ERT approach to the observation of solute breakthrough behaviour. The 3D inversion allows a direct estimate of voxel $\sigma_w$ whereas, in previous studies, the 2D inversion applied was limited to qualitative estimation of relative conductivity concentration (Binley et al., 1996; Slater et al., 2000). Furthermore, these previous efforts assumed a 2D conductivity model that is unlikely to faithfully represent solute transport mechanisms, and did not assess the validity of voxel breakthrough curves by comparison with direct measurements.

There is considerable potential for improvements in the 3D ERT estimation of voxel breakthrough curves. In this experiment, discrepancies in scale arose due to the relatively coarse parameterisation of the model

space in the inversion, dictated by constraints resulting from the number of electrical measurements and the computer processing speed. With further advances in both instrumentation and inversion algorithms, it will be possible to define smaller voxels (smaller support volume) on a denser grid than applied here. Of particular interest is a constraint on the inversion of a temporal sequence of ERT data in the time dimension. Our current inversion used a smoothness-constraint to minimise unrealistic image roughness in all three spatial dimensions. It is theoretically possible to apply a similar constraint on the time dimension by simultaneous inversion of all time sequential 3D datasets. We suspect that the rough character of some of the voxel breakthrough curves (see for example, Wells 9 and 13 in Fig. 5) is artificial and would be reduced by application of such an inversion procedure. Such a procedure, however, would require adequate a priori information of the extent of temporal smoothing. This may be estimated by hydrological models, although this removes the independent nature of any model comparison, such as in this study.

Other causes for the rough nature of certain ERT voxels include poor definition of the ERT FE model space (particularly edge effects) and translation of measurement errors into image voxel noise. However, we feel that, in this case, such errors are unlikely as the tank boundaries were accurately modelled with the 3D ERT FE mesh, and measurement errors were used to weight the relative effect of each measurement on the inversion result (noisier measurements were weighted less). One further problem in the definition of voxels breakthrough curves results from model equivalence. The essence of ERT inversion is numerically solving for a conductivity structure that provides a satisfactory fit between measured data and a theoretical dataset calculated for a defined conductivity structure. The inversion result is inherently non-unique, as there will be other 3D conductivity structures providing a satisfactory level of fit between the measured and modelled electrical data. Consequently, ERT voxel breakthrough curves are also non-unique.

A comparison of the sequence of ERT images with the predictions obtained from 3D solute transport modelling illustrates how ERT can identify relatively complex transport processes. There is general agreement between the ERT images and the model prediction. The ERT observed time of breakthrough in
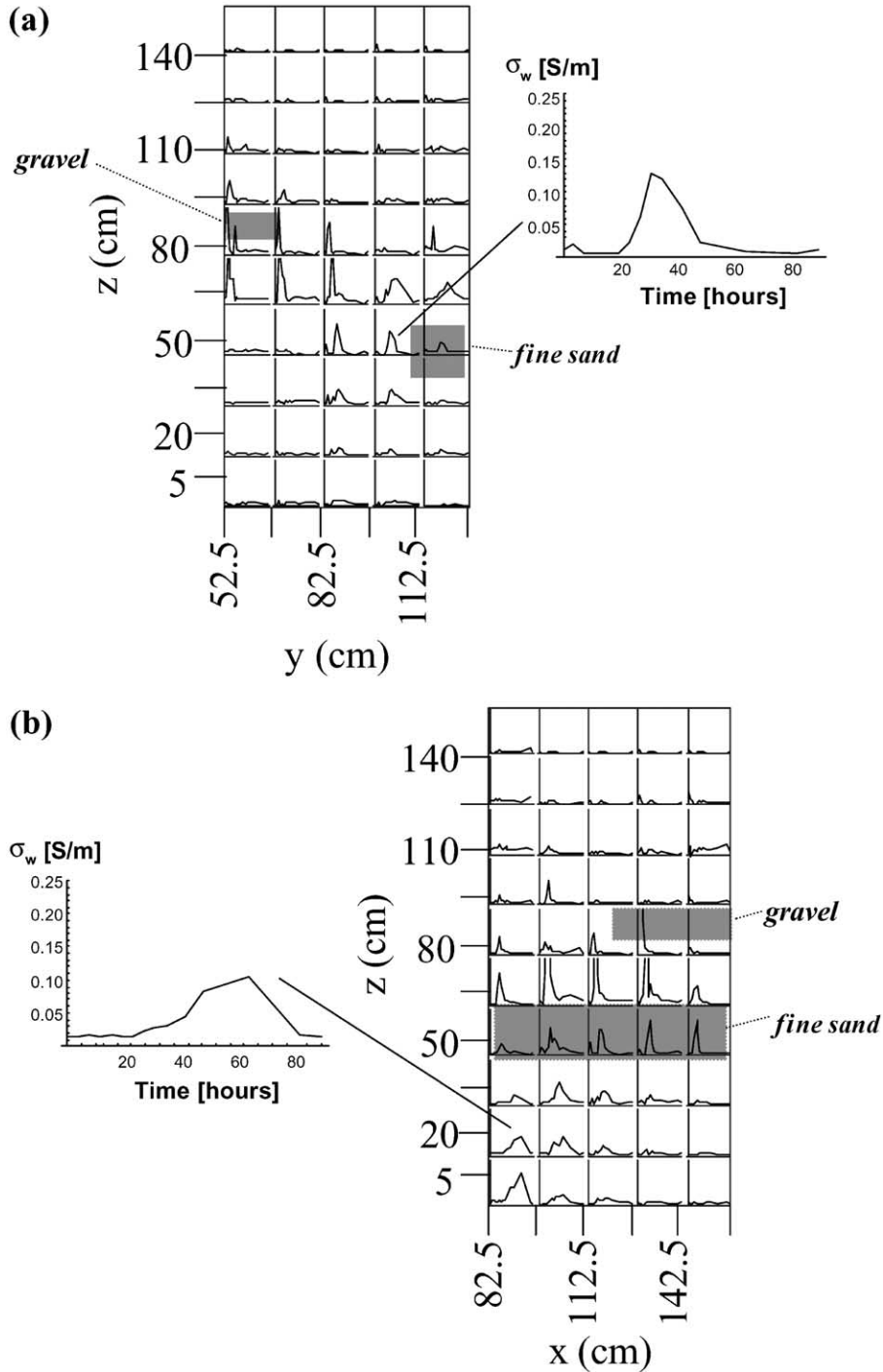
Fig. 8. (a) ERT-derived voxel breakthrough curves on image plane $x = 120$ cm. Note that the gravel layer is not continuous in the $x$ direction (see Fig. 1). (b) ERT-derived voxel breakthrough curves on image plane $y = 90$ cm. Note that the fine sand and gravel layers are offset from the image plane by approximately 20 cm and not continuous in the $y$ direction (see Fig. 1).

the gravel channel and in the medium sand is consistent with that predicted from the flow/transport modelling. However, the ERT images suggest greater complexity in solute transport behaviour than predicted by the modelling. One difference is the significant vertical transport suggested by ERT. The flow/transport modelling suggests that density-driven sinking was not the cause of this vertical transport. It was probably caused by transient gradients generated during tracer injection and/or unknown meso and macro heterogeneity. Insufficient information was available to incorporate this information into the transport modelling. A second difference is the more localised breakthrough in the sand observed with ERT, relative to the broader plume predicted from the flow/transport modelling. It is likely that tracer transport within the medium sand occurred along relatively permeable channels, a result of heterogeneity caused by the tank filling procedure. Late breakthrough observed above the fine sand layer may reflect the effects of macrostructure in the medium sand, transient vertical gradients and impeded vertical transport by the fine sand layer.

Transport models are often inaccurate, primarily due to insufficient available information on hydraulic properties and the geometry of the flow field (as in this case). Ultimately, it should be possible to use a spatially extensive 3D ERT dataset of voxel breakthrough curves to improve the calibration of a flow and transport model. In this study, the imaged volume contains 250 voxel breakthrough curves, each representing 3375 cm$^3$ of the tank. To illustrate, voxel breakthrough curves on image planes $x = 120$ cm and $y = 90$ cm are shown in Fig. 8a and b, respectively. Example voxels are magnified in an inset to show the scales on the axes. The voxels illustrate the variability in breakthrough response observed in the imaged volume. For example, early advective breakthrough, high $\sigma_w$ and sharp recession in the vicinity of the gravel channel contrast with more disperse, low $\sigma_w$ breakthrough observed within the sand, including above the fine-sand channel.

## 7. Conclusions

This study demonstrates the potential value of 3D ERT imaging for investigating flow and transport in a large-scale, heterogeneous, experimental tank. Reconstructed voxel bulk conductivity values were converted to equivalent fluid conductivity by assuming that surface conduction was small. This conversion was validated by the good agreement between ERT-estimated and direct measures of fluid conductivity. The pattern and timing of tracer breakthrough observed with ERT was in broad agreement with that predicted from 3D-coupled flow and transport modelling. However, ERT suggested more localised breakthrough in the sand and significant vertical transport of tracer, both of which were not predicted by the flow/transport modelling. This may reflect macrostructure resulting from non-uniform sand deposition during filling, and transient vertical gradients established during tracer injection. Insufficient information was available to include these effects in the flow/transport model. These results illustrate that 3D ERT imaging can resolve relatively complex flow and transport mechanisms.

One aspect of this study relates to the difficulty in creating well fitting hydrological transport models when the description of subsurface hydraulic properties and the flow field is incomplete (as it will inevitably always be). In this experiment, the electrical modelling indicates that solute transport is more complex than that predicted from the hydrological modelling based on the known macrostructure, hydraulic conductivity estimates and breakthrough curves at six wells. We suggest that electrical imaging of an injected tracer could be used to test the applicability of a hydrological model at a site characterised by inadequate hydrological data. Differences between transport behaviour predicted from the modelling and that observed with ERT could be used to improve the hydrological model. Ideally, it will be possible to use the large number of ERT-derived voxel breakthrough curves as direct input data to constrain the hydrological model. As emphasised, this hydrological application of ERT will require that the relationship between ERT-measured bulk conductivity and fluid conductivity is precisely known.

## References

Archie, G.E., 1942. The electrical resistivity log as an aid in determining some reservoir characteristics. Transactions of the American Institute of Mining, Metallurgical and Petroleum Engineers 146, 54–62.

Binley, A., Ramirez, A., Daily, W., 1995. Regularised image reconstruction of noisy electrical resistance tomography data. In: Beck, M.S., Hoyle, B.S., Morris, M.A., Waterfall, R.C., Williams, R.A. (Eds.), Process Tomography—1995. Proceedings of the 4th Workshop of the European Concerted Action on Process Tomography, Bergen, 6–8 April 1995, pp. 401–410.

Binley, A., Henry-Poulter, S., Shaw, B., 1996. Examination of solute transport in an undisturbed soil column using electrical resistance tomography. Water Resources Research 32, 763–769.

Daily, W., Owen, E., 1991. Cross-borehole resistivity tomography. Geophysics 56, 1228–1235.

Daily, W., Ramirez, A., LaBrecque, D., Nitao, J., 1992. Electrical resistivity tomography of vadose water movement. Water Resources Research 28, 1429–1442.

Daily, W., Ramirez, A., 1995. Electrical resistance tomography during in-situ trichloroethylene remediation at the Savannah river site. Journal of Applied Geophysics 33, 239–249.

LaBrecque, D.J., Ramirez, A.L., Daily, W.D., Binley, A.M., Schima, S.A., 1996a. ERT monitoring of environmental remediation processes. Measurement Science and Technology 7, 375–383.

LaBrecque, D.J., Miletto, M., Daily, W., Ramirez, A., Owen, E., 1996b. The effects of noise on Occam's inversion of resistivity tomography data. Geophysics 61, 538–548.

Lin, H.J., Richards, D.R., Talbot, C.A., Gour-Tsyh, Y., Cheng, J., Cheng, H., 1997. FEMWATER: A three-dimensional finite element computer model for simulating density-dependent flow and transport in variably saturated media. U.S. Army Corps of Engineers and Pennsylvania State University Technical Report CHL-97-12.

Slater, L., Binley, A., Brown, D., 1997. Electrical imaging of fractures using groundwater salinity change. Ground Water 35, 436–442.

Slater, L., Binley, A.M., Daily, W., Johnson, R., 2000. Cross-hole electrical imaging of a controlled saline tracer injection. Journal of Applied Geophysics: Special Issue—Environmental Geophysics 44, 85–102.

Versteeg, R., Birken, R., 2001a. An automated facility to study processes using 4D GPR. Proceedings of the Symposium on the Application of Geophysics to Engineering and Environmental Problems (SAGEEP), March 4–7, 2001, Denver.

Versteeg, R., Birken, R., 2001b. Imaging fluid flow and hydrologic conductivity using ground penetrating radar in a controlled setting. Proceedings of the Symposium on the Application of Geophysics to Engineering and Environmental Problems (SAGEEP), March 4–7, 2001, Denver.

Xu, B., Noel, M., 1993. On the completeness of data sets with multielectrode systems for electrical resistivity survey. Geophysical Prospecting 41, 791–801.